

## Large cylindrical polaron in orthorhombic SnSe: A theoretical study

Bogdan Guster , Vasilii Vasilchenko , Maryam Azizi , Matteo Giantomassi , and Xavier Gonze <sup>\*</sup>

*European Theoretical Spectroscopy Facility, Institute of Condensed Matter and Nanosciences, Université Catholique de Louvain, Chemin des étoiles 8, bte L07.03.01, B-1348 Louvain-la-Neuve, Belgium*



(Received 9 March 2023; revised 9 May 2023; accepted 16 June 2023; published 30 June 2023)

Due to its phenomenal thermoelectric properties, SnSe has received increased interest, triggering systematic studies of both electronic and vibrational properties and the associated coupling. Recent experimental work claims that orthorhombic SnSe sustains a one-dimensional large polaron with a dimension of about 2 nm. In search of its theoretical signature, we first establish the level of precision that can be reached in describing the electronic structure of SnSe by means of *ab initio* density functional and many-body perturbation theories. As the characterization of band extrema by means of effective masses plays a crucial role in determining polaron properties, we signal the existence of a broad variation of such quantity among the various *ab initio* methodologies employed and in the available experimental data. The impact of electron-phonon coupling is then analyzed by employing the recently developed generalized Fröhlich model as well as the nonadiabatic Allen-Heine-Cardona formalism, and their relative accuracy is rationalized. We found that, although the vast majority of band extrema in SnSe cannot sustain a large one-dimensional polaron with a radius as small as 2 nm, there is one case in which another type of polaron emerges, indeed one-dimensional, but with an unusual oscillating electronic density of an approximate real space period of  $\sim 3$  nm that evokes a stack of disks. Such type of polaron is obtained from two theoretical treatments: a fixed Gaussian ansatz for the polaron wave function and a variational approach, both within the Fröhlich formalism. We hypothesize that such cylindrical polaron might be found in other materials with extended, shallow double-well band extrema.

DOI: [10.1103/PhysRevMaterials.7.064604](https://doi.org/10.1103/PhysRevMaterials.7.064604)

### I. INTRODUCTION

The outstanding thermoelectric figure of merit of orthorhombic SnSe [1] has stimulated active experimental and theoretical investigations of its physical properties, paving the way for SnSe to become a paradigmatic case in the field of thermoelectricity [2–7]. SnSe is a versatile material exhibiting lattice phase transitions at high temperature [8], either driven from highly anharmonic phonon behavior [9–11] or near-infrared light-induced distortion [12], with strong electronic structure reorganization driven by chemical doping [13–15], pressure [16], strain [17], or temperature [18]. Rich polymorphism of SnSe [19,20] also gives rise to other avenues of study, such as the investigation of topological electronic structure in orthorhombic and rocksalt phases of the material [21,22].

Recently, by means of ultrafast electron spectroscopy, it has been hypothesized that orthorhombic SnSe accommodates two distinctive polarons, one large one-dimensional polaron and one small polaron with a three-dimensional character [23]. Since, at their core, polarons are quasiparticles (QPs) correlating the behavior of charge carriers with lattice deformations, understanding this behavior from a microscopic point of view builds upon the fundamental understanding of both the electronic and phononic structure, and the electron-phonon interaction (EPI) that ties the two ingredients.

Polarons, generally speaking, are pervasive QPs in many semiconductors and insulators [24]. This notion is far from new, tracing back to Landau and Pekar's works [25–27] decades ago. Polarons are traditionally separated in two categories: small or large, depending on whether or not their localization length is comparable with the crystal atomic periodicity. On this account, different theoretical models are suitable for accurately capturing the physical scenario. The Holstein model is appropriate in studying small polarons in which the discrete nature of the lattice is considered and the EPI is short-ranged [28,29]. In the case of large polarons, the Fröhlich model has been successful in apprehending the physical scenario in which the lattice discreteness and the electron-phonon coupling are treated in the long-wavelength limit, with lattice vibrations restricted to infrared-active optical phonon modes [30–35]. The standard Fröhlich model relies on the knowledge of the effective mass at the band extremum, the dielectric constant, and the long-wavelength polar phonon mode frequency. Recent developments have relied on first-principles approaches, built on accurate electronic and phononic band structures, as well as EPI computations [36–40]. Connections with the zero point renormalization (ZPR) of the electronic band gap have been established [36,40–45].

For the electronic structure of SnSe, the effort leaned toward understanding the behavior of the band gap and the subtle nature of the valence band extremum via ARPES studies [13–15,46–49] or, theoretically, via density functional theory (DFT) [2] or many-body perturbation theory (MBPT)

<sup>\*</sup>Corresponding author: [xavier.gonze@uclouvain.be](mailto:xavier.gonze@uclouvain.be)

within the  $G_0W_0$  approximation [50]. Although the understanding of the material electronic structure is utterly crucial, a systematic theoretical study in unveiling the fairly intricate band extrema and the corresponding effective masses associated with them is lacking. Up to now, electronic effective masses have been reported in several accounts, for selected extrema, yet for somewhat different circumstances, originating in experimental conditions (different temperatures for measurements) or methodological description, preventing fair comparison between published data [2,5,18,46–48,50].

In this paper, we employ state-of-the-art approaches to explore these properties and validate our findings against the available experimental data. Moreover, the recent experimental evidence of polarons motivates the careful analysis of EPI. We consequently determine the EPI effect on the electronic structure based on different methodologies. We first rely on a generalized Fröhlich model Hamiltonian for the determination of the polaron energy, shape, and localization length associated with the different band extrema present in the electronic structure. This is done using both a fixed Gaussian wave-function ansatz, as described in Refs. [51,52], as well as a numerical variational approach [53]. We also compute the ZPR to the electronic band gap in the nonadiabatic self-energy approach [41–43,45,54] using both the on the mass shell (OTMS) and the linearized solution of the QP equation.

Our results indicate that most of the band extrema cannot deliver a large polaron with a localization radius on the order of 3 nm, their localization length being much larger. Only the very flat profile of the electronic eigenenergy around  $\Gamma$  appears as a candidate to generate such a (not-so-)large polaron. Indeed, either right at  $\Gamma$  or at a shallow minima close to it, if  $\Gamma$  is only a saddle point, the effective mass can be quite large. However, its precise value, and even the location of the minimum, depend strongly on the theoretical methodology. Pushing further, the nonquadratic eigenenergy profile is fed in the Fröhlich Hamiltonian. We observe that if the flat profile has two separated minima, a new type of polaron appears, with an oscillating electronic wave function. By contrast, the electronic wave function found in the standard Fröhlich model is everywhere positive. The associated electronic charge density oscillates, with a period on the order of 3 nm in one of the methodologies.

The paper is organized as follows: In Sec. II, we summarize the state-of-the-art theoretical tools employed to describe the electronic structure, the phonon dispersion, and the EPI; in Sec. III, we describe the crystal structure; in Sec. IV, we perform a thorough investigation of the electronic structure, where we describe the different band extrema, and their relative energy difference depending on the employed methodology along with their corresponding effective masses; in Sec. V, we focus on the phonon dispersion, with particular emphasis on the eigenmodes that ultimately can contribute to the polaron formation in the Fröhlich picture; and, finally, we tie the fermionic and bosonic picture in Sec. VI, where we provide polaron formation energy, localization length, and effective masses in the framework of the Fröhlich model based on both a fixed Gaussian ansatz for the wave function as described in Refs. [51,52], as well as a variational approach recently developed in Ref. [53]. In this section, we engage

as well the nonadiabatic Allen-Heine-Cardona (AHC) formalism [41–43,54] to compensate for the shortcomings of the Fröhlich model in describing polaron formation energy, more commonly referred to as zero-point renormalization of the band gap. We conclude in Sec. VII.

## II. COMPUTATIONAL DETAILS

Calculations are performed using DFT as implemented in the ABINIT package [55–57]. It will be shown that crucial details of the electronic structure depend on the choice of the exchange-correlation (XC) energy functional, either directly or through the effect of optimized atomic positions and lattice parameters. In this respect, for all properties, we provide at least results based on the GGA-PBESol approximation [58] using the corresponding norm-conserving pseudopotentials provided by the PseudoDojo project [59,60]. However, given the sensitive dependence between polaron properties and electronic structure, an enlarged systematic approach towards electronic structure has been carried out employing different semiempirical van der Waals corrections, commonly known as D2 [61], D3 [62], and D3-BJ [63], or hybrid functionals, such as HSE06 [64].

A fully optimized crystal structure is obtained for each XC, with a corresponding tolerance on the maximum force of 5 meV/Å. The wave functions are expanded over a plane-wave basis set with a kinetic energy cutoff of 44 Ha. The Brillouin zone is sampled with a Monkhorst-Pack grid of  $8 \times 8 \times 4$  wave vectors for all cases, except for HSE06 calculations where a  $6 \times 6 \times 3$  wave-vector grid is used. To compute the energy dispersion with hybrid functionals, a Wannier interpolation scheme [65] is used for the states around the Fermi level. The effective masses are determined based on a second-order central finite difference.

Based on the converged electronic wave functions, Density Functional Perturbation Theory (DFPT) [57,66,67] has been used to obtain the phonon dispersion, the electronic effective masses (only in the case of PBESol XC), Born effective charges [68], and dielectric constants. For the phonon dispersion, a  $\Gamma$ -centered grid of  $8 \times 8 \times 4$  electronic wave function and dynamical matrices has been used (with much finer interpolation of phonon dispersion using interatomic force constants). For the other properties, a denser  $16 \times 16 \times 8$  mesh has been used. Given that effective mass calculations with DFPT are not available for all XC functionals, the agreement between DFPT and finite-difference approach was carefully checked for PBESol, and the converged finite difference parameters have then been used for all remaining XCs. It is worth noting that a particular treatment for determining effective masses is required when employing HSE06 XC. The hybrid calculation eigenvalues are indeed obtained over a reduced grid of wave vectors in the irreducible BZ. On top of these values, Wannier interpolation is used over a designated  $k$ -path around the (local or global) wave-vector extremum. This is then followed by a finite difference procedure implemented in ABIPY [55].

To correct for the limited description of the electronic structure provided by the Kohn-Sham (KS) formalism, the  $G_0W_0$  approximation has been employed to account for many-body interactions. Such one-shot  $G_0W_0$  calculations relied

either on the PBEsol self-consistent wave functions evaluated at the PBEsol geometry, denoted  $G_0W_0@PBEsol$ , or on the HSE06 self-consistent wave functions evaluated at the HSE06 geometry, denoted  $G_0W_0@HSE06$ . The QP corrections have been computed over an enlarged  $10 \times 10 \times 5$  electronic wave-vector grid and corrections were converged with respect to the fundamental band gap within 10 meV. The energy cutoff values for the dielectric matrix and the exchange part of the self-energy were set to 6 and 18 Ha, respectively. A set of 300 bands was included in the summation over states, and the extrapolar approximation proposed in Ref. [69] was used to accelerate convergence. The QP energy dispersion along the high-symmetry wave-vector path was produced using an interpolation scheme [70] based on 140 star functions per wave vector for both  $G_0W_0@PBEsol$  and  $G_0W_0@HSE06$ . The same approach was applied to determine the effective masses via finite differences.

In the case of phonon-induced QP corrections within the AHC formalism, the Kohn-Sham wave functions are calculated on a  $28 \times 28 \times 14$  wave-vector grid which contains the wave vector  $(9/28, 0.00, 0.00)$  that is very close to the band extremum of interest, located roughly at  $(0.32, 0.00, 0.00)$  across different XC functionals. The self-energy is computed with 80 bands and the Sternheimer equation is used to accelerate the convergence of the QP corrections with the number of empty states.

In the variational method for determining the polaron ground state [53] in the Fröhlich approximation, the QP wave function is converged using an anisotropic  $15 \times N \times 15$  wave-vector mesh with  $N$  increasing up to 105 to capture the fine features of the band minima along the  $\Gamma$ -Y direction. For the sake of convergence, the employed wave-vector meshes always include the extremal points, which is achieved by fixing the appropriate lattice parameters of the model that actually specify the size of the BZ hosting the polaronic wave function. These parameters can be adjusted irrespective of the actual lattice constants of the material, provided they define a BZ large enough for the wave function, since the Fröhlich model washes out the atomic character of a system and treats it as a continuous medium.

### III. CRYSTAL STRUCTURE

SnSe crystallizes in space group 62 (the  $Pbnm$  convention is used in this paper) with eight atoms in the unit cell and associated point group  $D_{2h}$ . The Sn atoms are covalently bonded in plane to Se forming slabs of corner-sharing trigonal pyramids, while out of plane ( $c$  direction) the slabs are weakly coupled through van der Waals interactions.

Crystal structure relaxations are performed using different XC functionals to assess their relative accuracy of DFT with respect to the experimental lattice parameters as presented in Table I. There is non-negligible variability in both experimental and theoretical data. Roughly speaking, PBEsol falls within 2.5% accuracy, VdW-D2: 1.5%, VdW-D3: 3%, VdW-D3(BJ): 2%, respectively, HSE06: 3%. This variability will play some role in the electronic structure results, especially at the level of the effective masses, see next section.

The atomic positions in SnSe can be expressed in terms of four internal parameters as detailed in Table II. At the level

TABLE I. Lattice parameters determined under a full relaxation with the indicated XC functional. For reference, the experimental values from different references are included.

XC	$a$ (Å)	$b$ (Å)	$c$ (Å)
PBEsol [58]	4.158	4.355	11.439
VdW-D2 [61]	4.195	4.382	11.635
VdW-D3 [62]	4.178	4.585	11.550
VdW-D3 (BJ) [71]	4.175	4.373	11.490
HSE06 [64]	4.148	4.582	11.860
Experiment [1]	4.135	4.440	11.490
Experiment [12]	4.120	4.300	11.310
Experiment [19]	4.182	4.387	11.540
Experiment [72]	4.153	4.450	11.502
Experiment [73]	4.190	4.460	11.570
Experiment [74]	4.153	4.445	11.501

of internal coordinates, the better-performing approaches are VdW-D3(BJ) and PBEsol, which fall reasonably close with respect to the experimental values, as shown in Table III. In addition to internal coordinates computed using fully relaxed PBEsol calculations (thus, relaxing the lattice parameters altogether), the internal positions obtained when fixing the lattice parameters at the experimentally determined ones from Ref. [74] are also provided, and denoted PBEsol[int].

### IV. ELECTRONIC STRUCTURE

The electronic structure of orthorhombic SnSe (referred to as SnSe from now on) has been at the center of a significant debate, especially focused on the nature of the valence band maximum (VBM), namely, whether or not its composition is "pudding-mold-like" [3,46]. The electronic band dispersion is presented in the ordinary DFT treatment using the semilocal XC PBEsol in Fig. 1 to allow for a first-hand qualitative evaluation. SnSe is a semiconductor with an indirect band gap presenting several close extrema.

The VBM situated, seemingly, along the  $\Gamma$ -Y direction presents a double hump decoupled from the underlying band due to an avoided crossing, situated at  $VB2 = (0.00 a^*, 0.35 b^*, 0.00 c^*)$  and  $VB3 = (0.00 a^*, 0.44 b^*, 0.00 c^*)$ . A closer inspection is provided in Fig. 1(c), where the band extrema

TABLE II. Reduced atomic coordinates of the eight atoms in the primitive cell of orthorhombic SnSe, in terms of the four internal parameters  $u_{Sn,y}$ ,  $u_{Sn,z}$ ,  $u_{Se,y}$ , and  $u_{Se,z}$ .

Atom	Reduced atomic coordinates		
	$x$	$y$	$z$
Sn1	1/4	$1/2 - u_{Sn,y}$	$1/2 + u_{Sn,z}$
Sn2	3/4	$1/2 + u_{Sn,y}$	$1/2 - u_{Sn,z}$
Sn3	3/4	$-u_{Sn,y}$	$-u_{Sn,z}$
Sn4	1/4	$u_{Sn,y}$	$u_{Sn,z}$
Se1	1/4	$u_{Se,y}$	$1/2 - u_{Se,z}$
Se2	3/4	$-u_{Se,y}$	$1/2 + u_{Se,z}$
Se3	3/4	$1/2 + u_{Se,y}$	$u_{Se,z}$
Se4	1/4	$1/2 - u_{Se,y}$	$-u_{Se,z}$



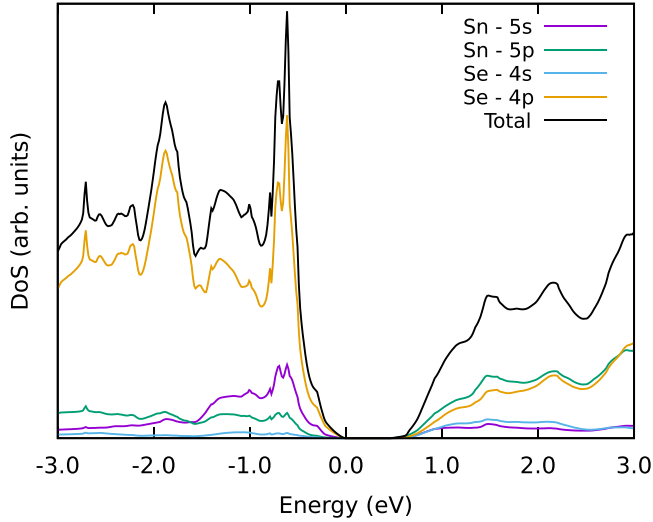


FIG. 2. Calculated electronic density of states of SnSe decomposed in orbital contributions.

decrease in the relative difference between the two band extrema in the CB is another one. A direct comparison with experiment can be made though at the level of the valence extrema ordering with the difference between global VBM and  $\Gamma$ -VB being in good agreement for both PBEsol (0.56 eV) and  $G_0W_0$ @PBEsol (0.75 eV) with respect to ARPES measurements (0.5 eV). The energy difference between the two VB humps (VB2 and VB3) is found to be 55 (24) meV under the PBEsol ( $G_0W_0$ @PBEsol) treatment, while in ARPES it is 29 meV. Experimentally, it has been proven that the relative difference between the different extrema is kept constant for the whole range of temperatures up to 600 K in which the orthorhombic phase is still stable [75]. A broader description of the relative energy difference between extrema of interest is presented in Table IV. The CBM position is shown in bold, while the VBM is VB2 unless otherwise bolded. Depending on the employed methodology, the CBM can be found either in a shallow extended minimum where the CBM is located at CB2 or in a parabolic band with the CBM located at CB1. In

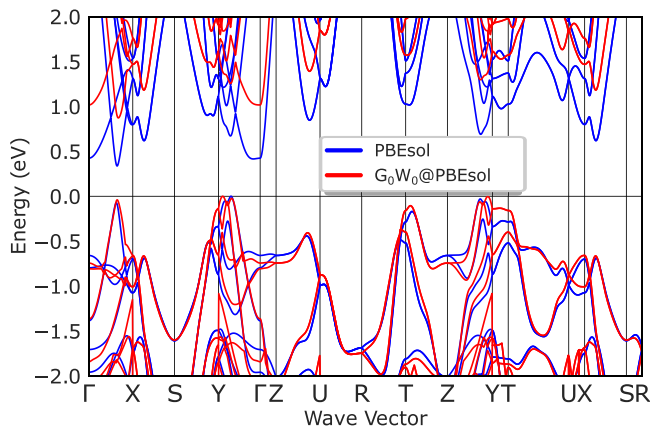


FIG. 3. Comparison of electronic bands dispersion between PBEsol and  $G_0W_0$ @PBEsol. Besides the obvious impact that  $G_0W_0$ @PBEsol has on the band gap, it is worth mentioning that  $G_0W_0$ @PBEsol shows a reordering of the double-hump extrema present in the VBM, having now VB3 as the VBM.

TABLE IV. Relative electronic eigenenergy difference with respect to the valence band maximum at VB2. All values are expressed in meV.  $E_g$  is the global (possibly indirect) gap. Results are obtained from different methodologies and a few geometries, namely, PBEsol at experimental geometry (PBEsol[exp] [74]), PBEsol at experimental lattice vectors [74], and relaxed internal coordinates (PBEsol[int]), different XC functionals at their own optimized geometries (PBEsol, D2, D3, and D3-BJ), hybrid functional at the corresponding optimized geometry (HSE06),  $G_0W_0$  from PBEsol wave functions, at PBEsol optimized geometry,  $G_0W_0$  from HSE06 wave functions, at HSE06 optimized geometry. The indicated extrema correspond to the conduction band at the zone center ( $\Gamma$ -CB), CB1 = (0.32  $a^*$ , 0.00  $b^*$ , 0.00  $c^*$ ), CB2 = (0.32  $a^*$ , 0.00  $b^*$ , 0.03  $c^*$ ), CB3 = (0.00  $a^*$ , 0.07  $b^*$ , 0.00  $c^*$ ), VB1 = (0.32  $a^*$ , 0.00  $b^*$ , 0.00  $c^*$ ), VB2 = (0.00  $a^*$ , 0.35  $b^*$ , 0.00  $c^*$ ), respectively, VB3 = (0.00  $a^*$ , 0.44  $b^*$ , 0.00  $c^*$ ) valid in the case of PBEsol XC functional (see Supplemental Material Table S1 for the complete set of extremal points [76]). The CBM position is shown in bold, while the VBM is VB2 unless otherwise bolded. Experimental CBM is attributed arbitrarily at the three  $\Delta$ CB locations (in parentheses) due to the lack of experimental data in the mentioned works.

Method	$\Delta$ CB1	$\Delta$ CB2	$\Delta$ CB3	$\Delta\Gamma$ -CB	$\Delta$ VB1	$\Delta$ VB3	$E_g$
PBEsol[exp]	<b>473</b>		604	599	-130	-41	473
PBEsol[int]	557	<b>374</b>	378	549	-159	-66	374
PBEsol	338	<b>334</b>	418	427	-73	-55	334
D2	473	<b>473</b>	558	577	-81	-17	473
D3	578	<b>575</b>	865	856	-198	-61	575
D3-BJ	<b>397</b>		479	484	-86	-59	397
HSE06	<b>1299</b>	1301	1437	1416	-299	<b>6</b>	1293
$G_0W_0$ @PBEsol	<b>896</b>		1031	1022	-16	<b>24</b>	872
$G_0W_0$ @HSE06	1378	1359	<b>1330</b>	1339	-183	-5	1330
Exp. [47]					-70	0	
Exp. [46]						-20	
Exp. [48]					-260	0	
Exp. [13]	(1200)	(1200)	(1200)		-300	0	1200
Exp. [75]	(860)	(860)	(860)		-215	-29	860

the case of VBM,  $G_0W_0$ @PBEsol and HSE06 reorganize the double-hump valence band with the VBM situated now at the VB3 point.

While most of the XC functionals perform reasonably well in reproducing the experimental lattice parameter along the  $c$  direction, HSE06 yields a larger deviation. Similarly HSE06 internal atomic coordinates deviate noticeably from experimental ones (see Table III). Hence, the electronic structure topology differs noticeably from the other ones. A comparison between PBEsol and HSE06 electronic structures is presented in Fig. 4. The pronounced change of lattice parameter drives a strong reorganization of the electronic structure. The double-hump VB shows a reordering compared to both theoretical and experimental data. A second major change is present in the secondary valence band extrema that are now located at  $\Gamma$  instead of being along the  $\Gamma$ -X direction.

Considering the different treatments of the electronic structure, the effective masses are evaluated for the several extrema, as presented in Table V.

We earlier noticed that the determination of the lattice parameters show variations of up to 3% depending on the

TABLE V. Effective mass determined for various electronic band extrema (local or global) present in the electronic structure obtained from different methodologies and a few geometries. Notations are the same as in Table IV. The effective masses are expressed in electron mass unit.

Method	Direction	$\Gamma$ - CB	CB1	CB2	CB3	VB1	VB2	VB3
PBEsol[exp]	(100)	0.9472	0.0792	0.0800		-0.0820	-0.3514	-0.1421
	(010)	55.9628	0.1391	0.1385		-0.1755	-0.1300	-0.1542
	(001)	0.0654	0.8856	0.5918		-0.2622	-0.5354	-2.0942
PBEsol[int]	(100)	0.9975	0.0701	0.0693	0.9598	-0.0750	-0.3109	-0.1304
	(010)	-3.2052	0.1323	0.1323	2.8195	-0.1670	-0.1210	-0.1644
	(001)	0.0659	0.8226	0.6746	0.0651	-0.2227	-0.3759	-1.4431
PBEsol	(100)	0.9116	0.0336	0.0512	0.8722	-0.0539	-0.2422	-0.0965
	(010)	-3.0050	0.1127	0.1253	2.6615	-0.1500	-0.1144	-0.1690
	(001)	0.0624	-3.1632	1.2504	0.0611	-0.3154	-0.5617	-1.2427
D2	(100)	1.1221	0.0676	0.0672	1.0178	-0.0711	-0.2158	-0.1376
	(010)	-2.2340	0.1307	0.1315	1.2926	-0.1359	-0.1678	-0.1644
	(001)	0.0749	-4.1357	1.8511	0.0721	-0.2804	-0.8119	-9.6217
D3	(100)	0.9999	0.1196	0.1191		-0.1300	-0.5396	-0.1976
	(010)	7.1832	0.1558	0.1570		-0.2332	-0.1682	-0.1877
	(001)	0.0708	0.6776	0.5434		-0.2878	-0.6118	-1.4329
D3-BJ	(100)	0.9086	0.0570	0.0576	0.8953	-0.0610	-0.2407	-0.1047
	(010)	-4.0922	0.1263	0.1261	2.5786	-0.1491	-0.1218	-0.1958
	(001)	0.0644	1.4908	0.6937	0.0634	-0.2914	-0.5136	-1.0809
HSE06	(100)	0.9225	0.1736	0.1742		-0.2269	-0.7466	-0.3056
	(010)	1.8390	0.1722	0.1729		-0.2557	-0.1765	-0.1951
	(001)	0.0927	0.5184	0.4948		-0.4185	-0.8328	-2.0015
$G_0W_0$ @PBEsol	(100)	0.8195	0.0477	0.0475	0.8641	-0.0610	-0.3029	-0.1001
	(010)	10.4202	0.1102	0.0993	1.5084	-0.1969	-0.1313	-0.1494
	(001)	0.0669	-1.0124	0.7556	0.0672	-0.3921	-0.6958	-1.2510
$G_0W_0$ @HSE06	(100)	0.9772	0.0546	0.0548	0.9131	-0.0561	-0.2253	-0.1083
	(010)	-1.9112	0.1184	0.1196	1.6242	-0.1375	-0.1013	-0.1403
	(001)	0.0600	-0.8610	7.7083	0.0582	-0.3397	-0.5257	-2.3934

used methodology. Moreover, the deviation might be larger along the slabs or perpendicular to them, which plays an important role, with an immediate impact on the effective masses. The effect is particularly strong in situations where the interslab separation is poorly described, as a consequence, giving rise to differences up to a factor of 2 in the electronic effective mass determination, except HSE06, which should

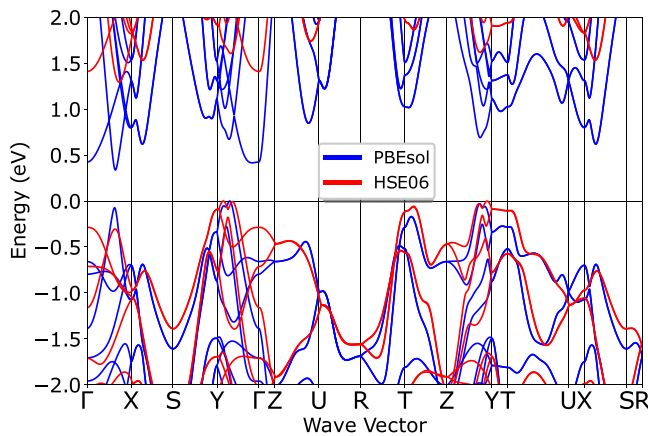


FIG. 4. Comparison of electronic bands dispersion between PBEsol and HSE06. Like in the  $G_0W_0$ @PBEsol many-body perturbative treatment, the inclusion of the exact exchange in the electronic structure description provided by HSE06 XC yields a reordering of the double-hump extrema present in the VBM.

be considered separately. It is thus apparent that the crystal structure is crucial in describing subtle electronic properties (see Supplemental Material Figs. S1 and S2 [76]). To further assess the relevance of the crystal structure, we shall restrict for a moment our comparison at the three PBEsol treatments of the effective masses in Table V: experimental structure (PBEsol[exp] [74]), PBEsol internal coordinate optimization with experimental lattice parameters [74] (PBEsol[int]), and fully relaxed structure with own functional (PBEsol). While for the  $\Gamma$  point, the effective masses at PBEsol[int] seem closer to the ones at PBEsol, the rest of the band extrema are neither closer to PBEsol[exp] nor to PBEsol, so we conclude in this regard that both internal coordinates and lattice vectors play a relevant role in the electronic band dispersion and the sensitive ordering of the band extrema. On the same note, we performed  $G_0W_0$ @HSE06 calculation (see Supplemental Material Fig. S3 [76]) and, most notably, the CBM is now situated at CB3, although we remain cautious about stamping this order as being the final one, given the extremely sensitive nature of the electronic dispersion.

A direct comparison with the theoretical results presented in this paper (see Table V) and other theoretical or experimental results (see Table VI) is available, although in this paper an optimized set of lattice parameters is used, while in the work of Ref. [50] the experimental lattice parameters are used. A second important point is that it is unclear in Ref. [50] on which XC functional the  $G_0W_0$  calculation is based on. At the experimental level, the data is available

TABLE VI. Published effective masses determined by various means, either experimental or theoretical, in view of comparing with Table V. No experimental data is available for the CB maximum.

Methodology	Direction	VB1	VB2	VB3	$\Gamma$	CB1
LDA [2]	(100)	0.24	0.30		0.16	
	(010)	0.16	0.18		0.12	
	(001)	0.46	0.78		0.50	
GGA [77]	(100)				0.85	
	(010)				2.12	
	(001)				0.069	
$G_0W_0$ [50]	(100)		0.31	0.12		0.11
	(010)		0.16	0.15		0.15
	(001)		0.74	0.90		2.40
ARPES [13]	(100)		0.17	0.16		
	(010)		0.25	0.21		
	(001)					
ARPES [46]	(100)		0.38	2-3		
	(010)		0.16	0.17		
	(001)		0.71	0.17		
ARPES [47]	(100)	0.19	0.21	0.19		
	(010)	0.13	0.13	0.12		
	(001)	0.31	0.42	0.58		
ARPES [48]	(100)	0.24	0.18	0.18		
	(010)	0.17	0.21	0.21		
	(001)		$\approx 2.5$	$\approx 2.5$		
ARPES [5]	(100)	0.20	0.25	0.20		
	(010)	0.13	0.17	0.13		
	(001)					
ARPES [18]	(100)		0.34			
	(010)		0.16			
	(001)		0.69			

in a somewhat incomplete fashion compared to the set of derivations of this paper, but the agreement is upheld up to a factor of 2 between both this paper's data and among different experimental measurements for VB1 and VB2 accounting for all employed methods. We account for the effects that spin-orbit coupling (SOC) might play in the determining the effective masses and we note that SOC is of no particular importance with the usual band splitting happening away from the band extrema (see Supplemental Material Fig. S4 [76]) and the effective masses are essentially degenerate (see, as an example, Supplemental Material Table S2 [76]). Restricting the comparison between PBEsol, D3-BJ, and  $G_0W_0$  methods and ARPES experimental results, the outcome is considerably more favorable, with the effective masses falling within 50% deviation from experiments. With this in mind, the window of precision of effective masses will have radical consequences on determining the polaron properties later.

Of particular importance are the selected points in the CB local extrema. It is worth emphasizing that  $\Gamma$ -CB shows a flat component of the band structure along the  $\Gamma$ -Y direction with a negative curvature in some of the XC treatments (PBEsol, D2, D3-BJ, or  $G_0W_0$ @HSE06) indicating that this is not a true local minimum in these cases, but then the minimum can be found along the high-symmetry path along  $\Gamma$ -Y. This behavior is absent in the  $G_0W_0$ @PBEsol where the flat component along  $\Gamma$ -Y has a positive curvature in turn. A similar behavior

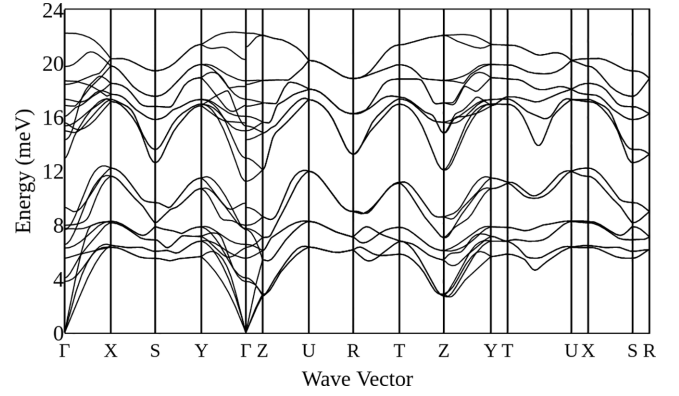


FIG. 5. Phonon dispersion in SnSe.

is observed in the case of CB1 in which case this is not the true extremum in PBEsol,  $G_0W_0$ @PBEsol, or  $G_0W_0$ @HSE06 treatments but rather is part of shallow band dispersion with a *hidden* minimum along the *c* direction at CB2.

To conclude this section, the lack of fool-proof systematic approaches for treating effective masses is underwhelming given the ramifications that it might have in estimating the electronic and polaronic properties of this potentially technologically suited material and other materials.

## V. PHONON STRUCTURE

The DFPT phonon dispersion obtained with the PBEsol-optimized crystal structure is presented in Fig. 5. The irreducible representations associated to the phonon modes ( $D_{2h}$ ) are separated in Tables VII and VIII based on their polar character. Altogether, the modes can be represented as  $\Gamma_{3N} = \Gamma_{\text{trans}} + 4A_g + 2B_{1g} + 2B_{2g} + 4B_{3g} + 2A_u + 3B_{1u} + 3B_{2u} + B_{3u}$ . As there is some arbitrariness about the notation of irreducible point group representation of this point group,

TABLE VII. Theoretical and experimental phonon eigenfrequencies for nonpolar modes, with their irreducible point group representation. Theoretical values are obtained within PBEsol XC treatment.

$\omega(\text{cm}^{-1})$		
Theoretical	Experimental [78]	Symmetry
30.57	33	$A_g$
32.46	37	$B_{1g}$
44.51		$A_u$
52.87	57	$B_{2g}$
61.71		$B_{3g}$
62.41		$B_{3g}$
63.79	70	$A_g$
104.18	108	$B_{1g}$
120.51		$A_u$
123.72	130	$A_g$
129.47	133	$B_{2g}$
139.41		$B_{3g}$
150.81	150	$A_g$
179.40		$B_{3g}$

TABLE VIII. Theoretical and experimental phonon eigenfrequencies for polar modes, depending on the limiting wave-vector direction, with their irreducible point group representation. Theoretical values are obtained within PBEsol XC treatment. Experimental TO frequencies correspond to the doubly degenerate theoretical values, while experimental LO frequencies correspond to the non-degenerate theoretical values.

$\omega(\text{cm}^{-1})$					Symmetry
(100)	(010)	(001)	TO [73]	LO [73]	
50.63	50.63	51.11	$56 \pm 5$	$57 \pm 5$	$B_{1u}$
75.18	77.88	75.18	$80 \pm 5$	$85 \pm 5$	$B_{2u}$
150.57	90.44	90.44	$96 \pm 5$	$172 \pm 5$	$B_{3u}$
115.69	147.93	115.69	$123 \pm 5$	$149 \pm 5$	$B_{2u}$
125.79	125.79	135.30	$130 \pm 5$	$141 \pm 5$	$B_{1u}$
135.84	135.84	172.96	$142 \pm 10$	$191 \pm 10$	$B_{1u}$
149.08	163.97	149.08	$150 \pm 5$	$180 \pm 5$	$B_{2u}$

we take the convention that the  $B_{1g}$  and  $B_{1u}$  are left invariant under the action of the  $C_{2z}$  binary axis,  $B_{2g}$  and  $B_{2u}$  are left invariant under the action of the  $C_{2y}$  binary axis, and  $B_{3g}$  and  $B_{3u}$  are left invariant under the action of the  $C_{2x}$  binary axis. The phonon frequencies are in good agreement with experimental values having a deviation of up to  $6 \text{ cm}^{-1}$  [78], the deviation being slightly larger towards the higher energy modes where the harmonic approximation might not be suitable anymore. In Table VII, a comparison between the theoretical and available experimental data for Raman active ( $g$ ) phonon modes is presented. In the case of infrared active ( $u$ ) modes, especially relevant in the case of the Fröhlich model, the phonon frequencies and their directional dependence are presented in Table VIII. Generally, the phonon mode decomposition agrees with experimental studies [78]. It does not agree with another theoretical work [18] where the attribution of polar modes is questionable and where the notation of irreducible representations does not even correspond to the one for the orthorhombic SnSe  $D_{2h}$  point group.

In the Fröhlich model, only polar phonon modes couple to the electronic degrees of freedom. They are distinctive due to the nonanalytic directional behavior of the frequencies for  $q \rightarrow \Gamma$  originating in the long-range character of the Coulomb interaction (see Table VIII). The origin of large polarons is usually ascribed to such long-range Coulomb characteristics, at variance with small polarons that stem from atomically localized interactions.

Two quantities characterize such long-range interaction with these modes: the Born effective charge tensors and the dielectric tensors. Born effective charges, shown in Table IX, are in good agreement with previous calculations [79], although presented in a somewhat incomplete manner in the latter reference. The Born effective charge tensor has off-diagonal elements, and moreover is nonsymmetric. Indeed, the local symmetry at one atom site is not orthorhombic, unlike the crystal. Also, the two derivatives defining the Born effective charge tensor, namely, with respect to the electric field, and with respect to atomic positions, are not equivalent.

The electronic dielectric tensor,  $\epsilon^\infty$ , is diagonal, with values (29.85, 24.62, 21.97). The static dielectric tensor,  $\epsilon^0$ , is also diagonal, with values (82.45, 52.23, 41.97). For

TABLE IX. Born effective charges of SnSe determined within the PBEsol XC functional. Columns refer to derivatives with respect to the electric field and lines to derivatives with respect to atomic positions, in atomic units.

Atom	Wyckoff	Born effective charges (e)			
Sn(1)	4c	$\partial/\partial\epsilon_x$	$\partial/\partial\epsilon_y$	$\partial/\partial\epsilon_z$	
		$\partial/\partial R_x$	4.645893	0	0
		$\partial/\partial R_y$	0	4.048746	0.005551
		$\partial/\partial R_z$	0	0.553763	3.896242
Se(1)	4c	$\partial/\partial\epsilon_x$	$\partial/\partial\epsilon_y$	$\partial/\partial\epsilon_z$	
		$\partial/\partial R_x$	-4.645893	0	0
		$\partial/\partial R_y$	0	-4.048746	0.497380
		$\partial/\partial R_z$	0	0.511980	-3.896242

further reference, their combination,  $\epsilon^* = ((\epsilon^\infty)^{-1} - (\epsilon^0)^{-1})^{-1}$  has diagonal values (46.80, 46.59, 46.09). While  $\epsilon^\infty$  and  $\epsilon^0$  present some noticeable anisotropy along the different crystallographic directions,  $\epsilon^*$  varies by less than 2%. These values deviate somewhat from experimental values, as reported in Chandrasekhar *et al.* [73] with  $\epsilon^0 = (62 \pm 6, 45 \pm 5, 42 \pm 5)$  and  $\epsilon^\infty = (17 \pm 2, 13 \pm 2, 16 \pm 2)$ . The theoretical values are not expected to be very accurate due to the band-gap underestimation in PBEsol. Indeed, a smaller band gap gives rise to a larger high-frequency dielectric response. However, experimental  $\epsilon^\infty$  is inferred from fitting and extrapolation of data at frequencies much lower than the band gap, a procedure also prone to significant uncertainty. In the following, we will stick, consistently with our approach, with the theoretical values. Irrespective of the used  $\epsilon^*$ , the polaron radii of the different band extrema in most cases would still be considerably larger than the experimental findings as we will see later in Table XI.

## VI. ELECTRON-PHONON EFFECTS

The impact of EPI can be evaluated using various theoretical methodologies, depending on the sought quantity, and whether one aims at an accurate quantitative picture or a more qualitative one. In the present paper, we analyze the polaron formation energy and the polaron spatial characteristics, for which different methodologies are indeed delivering complementary information.

The polaron formation energy (also known as ZPR of the band edge) is addressed based on two approaches: the nonadiabatic AHC theory and the Fröhlich model based on parameters

TABLE X. Polaron formation energy (ZPR) in meV stemming from various electronic band extrema (local or global) present in the electronic structure. The PBEsol XC functional is used.

Method/extremum	$\Gamma$ -CB	CB1/2	VB1	VB2	VB3
OTMS	-4.6	-12.3	9.2	7.8	9.1
LQPE	-4.7	-12.8	9.4	8.0	9.5
generalized Fröhlich	-4.4	-4.4	3.9	5.7	6.1
Gaussian/PBEsol		-0.10	0.08	0.16	0.20
Gaussian/ $G_0W_0$ @PBEsol	-0.31	-0.08	0.10	0.19	0.15

TABLE XI. Polaron localization lengths along different crystallographic directions for the different electronic band structure extrema from a Gaussian ansatz. Dimensions are expressed in Å. In this scenario, the polaron has a triaxial ellipsoidal shape.

Method	Dir	$\Gamma$ -CB	CB2	CB3	VB1	VB2	VB3
PBEsol	$x$		882.02	180.84	1063.03	387.69	426.90
	$y$		630.72	123.52	726.29	509.78	372.98
	$z$		284.31	488.67	589.26	288.73	133.81
$G_0W_0$	$x$	154.98	1037.46		839.46	317.46	548.81
	$y$	65.17	788.26		546.98	430.82	472.85
	$z$	403.29	389.28		430.26	237.14	225.14

extracted from first-principles calculations. The latter can also be used to examine the spatial characteristics of the polaron in the strong-coupling limit.

In the nonadiabatic AHC approach, the ZPR is derived from the electron-phonon self-energy obtained within a many-body perturbative approach. In the lowest order of perturbation theory, two contributions to the self-energy arise, the frequency-dependent Fan-Migdal term and the static Debye-Waller term [36]:

$$\Sigma_{\mathbf{k}n}^{\text{EPH}}(\omega) = \Sigma_{\mathbf{k}n}^{\text{FM}}(\omega) + \Sigma_{\mathbf{k}n}^{\text{DW}}. \quad (1)$$

The AHC approach takes into account the details of phonon modes and EPI over the entire Brillouin zone, computed from first principles, at variance with the Fröhlich approach, which relies only on zone-center quantities.

In the standard Fröhlich model, indeed, one assumes a single isotropic electronic band, with parabolic dispersion described by its corresponding effective mass  $m^*$ , and one dispersionless longitudinal zone-center optical phonon mode of frequency  $\omega_{\text{LO}}$ , both being coupled by a macroscopically screened Coulomb interaction. Obviously, this simplified isotropic one-band one-phonon picture does not apply in the case of SnSe, with seven infrared active modes and several electronic band extrema that could hold the formation of a polaron. The effective masses at band extrema sometimes span two degrees of magnitude along different crystallographic directions.

Considering all this, the generalized Fröhlich model developed by Miglio *et al.* [54] is a much better starting point to obtain the ZPR with a simple methodology compared to the AHC one. We will indeed obtain the ZPR from such a generalized model in the weak-coupling limit. For some band extrema, the agreement between AHC and the generalized Fröhlich approach is fair, between 10% and 20%, while it is only qualitative for some others.

The localization and shape of a polaron are well-defined in the strong-coupling limit but do not emerge from the weak-coupling limit. We will rely on formulas valid in the strong-coupling limit to tackle the comparison with experiment, thus working also in a more qualitative approach. In this respect, we will simplify the generalized Fröhlich model thanks to directionality-averaged dielectric tensors, and examine polaronic characteristics, first using a Gaussian wave-function ansatz, and then using a fully variational numerical approach. Both deliver a unique kind of large polaron,

whose electronic wave function oscillates in real space. The corresponding electronic charge density vanishes on surfaces separating sign changes in the electronic wave function. Thus, in this type of polaron, the electronic charge density can be thought of stacked disks given the not-so-large polaron localization length out-of-plane, while being much more delocalized in plane. The period of oscillations matches the characteristic length from experimental observations.

### AHC model ZPR

The QP correction due to EPI, based on the nonadiabatic AHC self-energy Eq. (1), can be obtained within two different treatments of the self-energy, namely, the OTMS and the linearized QP equation (LQPE). In OTMS, the QP correction is given by the real part of the EPI self-energy evaluated at the bare Kohn-Sham eigenvalue, so

$$\epsilon_{\mathbf{k}n}^{\text{QP}} = \epsilon_{\mathbf{k}n} + \text{Re}(\Sigma_{\mathbf{k}n}^{\text{EPH}}(\epsilon_{\mathbf{k}n})), \quad (2)$$

while in the LQPE, the correction is provided on the basis of a Taylor expansion of the self-energy around the bare KS eigenvalue.

Table X gathers our computed values, from both OTMS and LQPE. The two approximations show good agreement among each other for both CBM and VBM QP corrections within PBEsol XC. The polaron formation energies from both methods are relatively low, with absolute values below 10 meV. Thus the lack of ARPES experimental evidence is justifiable in this regard since it would require a relatively high resolution to detect features of this order of magnitude, if any. Also, when compared with Table IV, the QP corrections leave the ordering of the band extrema unchanged.

### A. Generalized Fröhlich model ZPR

The generalized Fröhlich model, delivering the zero-point renormalization denoted ZPR<sup>gFr</sup> [54], is parameterized using PBEsol results. At the lowest order of perturbation theory (weak coupling limit), the ZPR<sup>gFr</sup> for the different local minima of the CB can be calculated from the following expression (similarly for the valence band maxima, with a sign change):

$$\begin{aligned} \text{ZPR}_c^{\text{gFr}} = & - \sum_{jn} \frac{1}{\sqrt{2}\Omega_0 n_{\text{deg}}} \int_{4\pi} d\hat{\mathbf{q}} (m_n^*(\hat{\mathbf{q}}))^{1/2} \\ & \times (\omega_{j0}(\hat{\mathbf{q}}))^{-3/2} \left( \frac{\hat{\mathbf{q}} \cdot \mathbf{p}_j(\hat{\mathbf{q}})}{\epsilon^\infty(\hat{\mathbf{q}})} \right)^2, \end{aligned} \quad (3)$$

with  $m_n^*(\hat{\mathbf{q}})$  being the direction-dependent effective mass,  $\omega_{j0}(\hat{\mathbf{q}})$  being the direction-dependent infrared active phonon mode frequency at the  $\Gamma$  point, and  $\epsilon^\infty(\hat{\mathbf{q}})$  being the direction-dependent electronic dielectric tensor.

The generalized Fröhlich ZPR has the same order of magnitude as the polaron ground-state energy values provided by AHC methods. For  $\Gamma$ -CB, VB2, and VB3, they differ by less than a factor of 2, which suggests that the main contribution to the ZPR originates from the coupling of the long wavelength longitudinal optical phonons with the electronic structure. The agreement for other extrema is more qualitative, but still speaks in favor of pursuing with the Fröhlich model.

### B. Polaron localization lengths based on a Gaussian ansatz

The localization of a polaron and its associated charge distribution are well-defined in the strong-coupling limit. In the two coming sections, the generalized Fröhlich model will be slightly simplified by considering directionally averaged dielectric tensors (low-frequency and high-frequency), together with the strong-coupling limit, while keeping details (e.g., anisotropy and possible flatness) of the electronic structure at each of its extrema. In the present section, the expansion of the electronic eigenenergy is assumed quadratic, hence, represented by the effective mass tensor, while in the next section, a quartic expansion will be used to model the behavior of the CB around  $\Gamma$ .

An initial attempt to derive a localization length for a polaron was done by Landau and Pekar, in their seminal polaron work [25,26]. They considered the strong-coupling limit. The approach is based on the variational principle, whereby the energy associated to a normalized trial wave function  $\phi(\mathbf{r})$  [or  $\phi(\mathbf{k})$  in reciprocal space] combines an electronic kinetic energy part and a coupled electron-phonon and phonon part. Explicitly, when applied to the standard Fröhlich model (so, isotropic electronic dispersion),

$$E_P[\phi] = E_{el}[\phi] + E_{ep}[\phi], \quad (4)$$

where the electronic energy writes

$$E_{el}[\phi] = \int d\mathbf{k} \frac{\mathbf{k}^2}{2m^*} |\phi(\mathbf{k})|^2, \quad (5)$$

while the electronic density, obtained from  $\phi$  in real space,

$$\rho(\mathbf{r}) = |\phi(\mathbf{r})|^2, \quad (6)$$

induces a response of the polarizable medium, obtained mathematically by considering its Fourier transform

$$\rho(\mathbf{k}) = \frac{1}{(2\pi)^{3/2}} \int d\mathbf{r} \rho(\mathbf{r}) e^{i\mathbf{k}\mathbf{r}}, \quad (7)$$

and building the associated electron-phonon and phonon energy

$$E_{ep}[\phi] = - \int d\mathbf{k} \frac{4\pi}{2k^2\epsilon^*} \rho^*(\mathbf{k})\rho(\mathbf{k}), \quad (8)$$

with the dielectric constant

$$(\epsilon^*)^{-1} = (\epsilon^\infty)^{-1} - (\epsilon^0)^{-1}. \quad (9)$$

The electron wave function is frozen, as well as the deformation of the polarizable medium. Hence, in this strong-coupling scenario, one works in an adiabatic approximation, in which the electron and phonon parts are explicitly correlated, albeit frozen.

Different simple trial wave functions can be found in the literature, giving analytical results. The convenient Gaussian trial wave function used by Landau and Pekar [25,26,80] writes

$$\phi(\mathbf{r}) = \left( \frac{1}{\sqrt{\pi}a_P} \right)^{3/2} \exp\left( -\frac{r^2}{2a_P^2} \right). \quad (10)$$

Solving the minimization problem, the localization length is obtained in terms of the electron effective mass  $m^*$  and the

dielectric constant  $\epsilon^*$ , defined in Eq. (9):

$$a_P = \frac{3}{2} \sqrt{2\pi} (m^*)^{-1} \epsilon^*. \quad (11)$$

For many electronic band extrema in SnSe, the dispersion is highly anisotropic, differing sometimes by more than one order of magnitude along the three crystallographic directions. Equation (5) needs to be generalized, following Ref. [51], which gives

$$E_{el}[\phi] = \int d\mathbf{k} \left( \frac{k_x^2}{2m_x^*} + \frac{k_y^2}{2m_y^*} + \frac{k_z^2}{2m_z^*} \right) |\phi(\mathbf{k})|^2. \quad (12)$$

By contrast, as mentioned in Sec. VI, the dielectric tensor  $\epsilon^*$  is only weakly anisotropic. Thus, we will keep the other equations unchanged. The averaged value  $\epsilon^* = 46.49$  will be used in what follows.

Similarly, the trial wave function should allow for an ellipsoidally shaped polaron [51],

$$\phi(x, y, z) = \left( \frac{1}{\pi^{3/2} a_{Px}^2 a_{Py}^2} \right)^{1/2} \times \exp\left( -\frac{1}{2} \left( \frac{x^2}{a_{Px}^2} + \frac{y^2}{a_{Py}^2} + \frac{z^2}{a_{Pz}^2} \right) \right), \quad (13)$$

where  $a_{Px}$ ,  $a_{Py}$ , and  $a_{Pz}$  are the polaron localization lengths along the  $x$ ,  $y$ , and  $z$  directions, and  $a_P$  is the spherical average radius of the polaron, defined as follows:

$$a_P^3 = a_{Px} a_{Py} a_{Pz}. \quad (14)$$

As described in Ref. [51], this leads to solving numerically a system of equations to find the three  $a_{Pi}$  values,

$$\frac{1}{m_i^*} = - \frac{2a_{Pi}^3}{\epsilon^* (2\pi)^{1/2}} \frac{\partial \langle a_{Pd}^{-1} \rangle_{4\pi}}{\partial a_{Pi}}, \quad (15)$$

with  $\langle a_{Pd}^{-1} \rangle_{4\pi}$  being the angular average of the inverse of localization lengths.

In determining the polaron radius, the coupled set of Eq. (15) are solved for each extremum selected in the electronic band structure for two treatments: PBESol and  $G_0W_0$ @PBESol. The polaron formation energy is presented in Table X, while the polaron localization lengths are presented in Table XI.

The smallness of the polaron formation energy obtained in this strong-coupling limit, compared to the one obtained in the weak-coupling energy, signals the dominance of the Fan-Migdal self-energy over the polaronic self-energy, in the approach outlined recently by Lafuente-Bartolome *et al.* in their unified approach to polaron and phonon-band structure renormalization approach [39]. Both have to be taken into account in such a formalism, while one or the other are present in either the weak-coupling or the strong-coupling approach.

Although the formation energy is clearly dominated by the Fan-Migdal self-energy, there is no localization induced by such term *per se*. Localization only appears to be induced linked to the polaron self-energy, hence our belief that the strong-coupling approach will deliver a qualitatively correct evaluation of the localization radius for the polarons attached to the different band structure extrema.

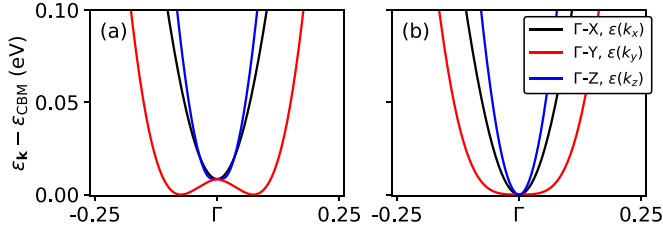


FIG. 6. Cross sections of the SnSe conduction band near the  $\Gamma$  point for PBEsol functional with (a) optimized or (b) experimental lattice parameters and atomic positions (PBEsol and PBEsol[exp]). Black, red, and blue lines denote paths from  $\Gamma$  to X, Y, and Z points of the Brillouin zone, respectively. The values on the horizontal scale specify the fraction from  $\Gamma$  to X, Y, or Z, with respect to the corresponding zone boundary.

Within this framework, the value closest to the large polaron radius found experimentally appears in the  $G_0W_0@PBEsol$  treatment of the CB minimum at the  $\Gamma$  point along the  $b$  direction, roughly  $65 \text{ \AA}$ .

Yet it is still a factor of nearly 4 higher than the experimental value,  $18.7 \text{ \AA}$  [23]. All other analyzed extrema present a much larger polaron radius. This was expected, given their relatively small effective mass, irrespective of the direction considered. However, the CB states at or around  $\Gamma$  are not at the CB global minimum, that, according to Table IV, is located either at CB1 or at CB2. Still, the energy difference between the CB global minimum and the CB at  $\Gamma$  is lower than  $0.15 \text{ eV}$  in most theoretical methods, a rather small value, that should not prevent the creation of such polarons. So, the characterization of a hypothetical polaron, stemming from the electronic states around  $\Gamma$  cannot be ruled out, while the other possibilities seem unrealistic.

As a conclusion, adopting a fixed Gaussian ansatz in the strong-coupling limit delivers a rather simple message: the small or even very small effective masses found for most extrema cannot yield a polaron with extent on the order of the ones found experimentally, with one noticeable exception of a polaron created from the CB states at or around  $\Gamma$ . Still, the smallest radius of such a polaron is found within a factor of nearly 4 from the largest experimental value. This might be ascribed to the inherent approximations in this theoretical approach.

In this respect, in the next subsection, we use a much more accurate technique, and take into account the peculiar shape of the band dispersion in the  $\Gamma$  neighborhood.

### C. Polaron wave functions based on a variational approach

As demonstrated in Ref. [53], the Gaussian wave function is an excellent ansatz for the Fröhlich model in the strong-coupling limit. However, the PBEsol dispersion of the SnSe CB near the  $\Gamma$  point significantly deviates from the quadratic behavior assumed in the Fröhlich model (see Fig. 6). Hence, a more careful approach is needed to characterize the polaron formation in the vicinity of the  $\Gamma$  point.

To obtain the polaron formation energy  $E_P$  and wavefunction  $\phi$ , we minimize the variational polaron equation of

Ref. [53]:

$$E_P(\mathbf{A}, \mathbf{B}) = \frac{1}{N_p} \sum_{\mathbf{Gk}} |A_{\mathbf{Gk}}|^2 \varepsilon_{\mathbf{Gk}} + \frac{1}{N_p} \sum_{\mathbf{Gq}} |B_{\mathbf{Gq}}|^2 \omega_{\text{LO}} - \frac{1}{N_p^2} \sum_{\mathbf{Gk}} \sum_{\mathbf{G'k'}} (A_{\mathbf{Gk}}^* A_{\mathbf{G'k'}} B_{(\mathbf{G}-\mathbf{G}'+\mathbf{U})(\mathbf{k}-\mathbf{k}'-\mathbf{U})} \times g^{\text{Fr}}(\mathbf{G}-\mathbf{G}'+\mathbf{k}-\mathbf{k}') + (\text{c.c.})). \quad (16)$$

The minimization is performed with respect to the electronic coefficients  $A_{\mathbf{Gk}}$  that define the polaronic wave function in the basis of Bloch states,

$$\phi(\mathbf{r}) = \frac{1}{N_p \sqrt{\Omega_0}} \sum_{\mathbf{Gk}} A_{\mathbf{Gk}} e^{i(\mathbf{k}+\mathbf{G})\cdot\mathbf{r}}, \quad (17)$$

with the vibrational coefficients  $B_{\mathbf{Gq}}$  being coupled with  $A_{\mathbf{Gk}}$  through the expression

$$B_{\mathbf{Gq}} = \frac{1}{N_p} \sum_{\mathbf{Gk}} A_{(\mathbf{G}'+\mathbf{G}-\mathbf{U})(\mathbf{k}+\mathbf{q}+\mathbf{U})}^* \frac{g^{\text{Fr}}(\mathbf{G}'+\mathbf{q})}{\omega_{\text{LO}}} A_{\mathbf{Gk}}. \quad (18)$$

In the equations above, a Born-von Karman supercell consisting of  $N_p$  primitive cells of volume  $\Omega_0$  hosts a polaron and is defined by the size of a corresponding  $\mathbf{k}$  mesh in reciprocal space. Parameters of the system, required to initialize the minimization, are the electronic dispersion  $\varepsilon_{\mathbf{Gk}}$ , the LO phonon mode energy  $\omega_{\text{LO}}$  and the Fröhlich electron-phonon matrix elements  $g^{\text{Fr}}(\mathbf{q})$ , which depend on the value of the dielectric constant.

In SnSe, around  $\Gamma$ , the first-principles electronic dispersion is highly sensitive to the calculation methodology. In Fig. 6, one can see two distinct behaviors of the CB near the  $\Gamma$  point: along the Y- $\Gamma$ -Y direction, it either (a) exhibits two minima or (b) is strikingly flat, while the dispersion along the other directions can be considered as parabolic. The double-well shape is found for the PBEsol functional with full geometry relaxation, as well as for the D2 and D3(BJ) XC functionals with their own geometries, and  $G_0W_0@PBEsol$ , while the other considered methods lead to the second, flat-band scenario. As shown in Table V, the heaviest effective masses in the Y- $\Gamma$ -Y direction are given either by PBEsol with experimental lattice parameters and atomic positions (PBEsol[exp]) or by  $G_0W_0$ , and these methods can be viewed as representatives of the flat-band case. Hence, to characterize a polaron, we consider both possible energy profiles: double well (PBEsol) and flat band (PBEsol[exp] or  $G_0W_0@PBEsol$ ). In any case, to parametrize Eq. (16), we use the sum of the electronic bands along three directions, as shown in Fig. 6:

$$\varepsilon(\mathbf{k}) = \varepsilon_x(k_x) + \varepsilon_y(k_y) + \varepsilon_z(k_z). \quad (19)$$

As mentioned previously, the dielectric constant  $\varepsilon^*$  is assumed isotropic and has a value of 46.49 further on. The phonon parameters are taken from the previously mentioned first-principles values.

As a result, the characteristic of the polaron differs significantly depending on the considered dispersion. While in reciprocal space the flat-band polaronic wave function is an ellipsoid, the double-well profile reveals another shape that has two distinct peaks at each of the minima, as shown in Fig. 7.

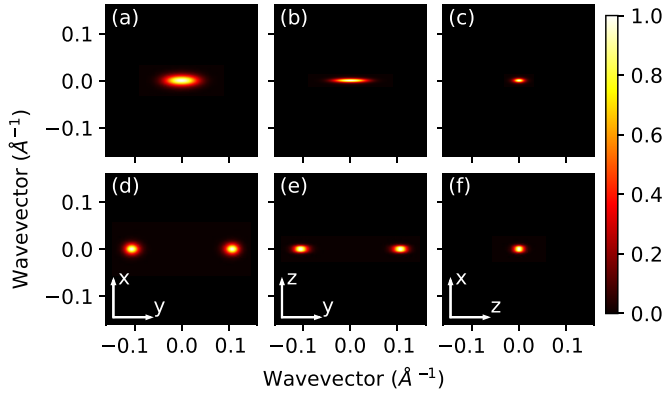


FIG. 7. Cross section of the reciprocal space polaronic wave function for the (a)–(c) flat-band PBEsol-exp and (d)–(f) double-well PBEsol-relaxed electronic dispersion. In all panels, the third coordinate is perpendicular to the plane and set to 0, except (c), where  $y$  is at one of the two minima.

Fourier transform allows one to obtain the corresponding polaronic density in real space, illustrated in Fig. 8. The flat-band scenario leads to a delocalized polaron, with PBEsol[exp] showing less pronounced delocalization in the flat-band direction than with  $G_0W_0$  parametrization (see Supplemental Material Fig. S5 [76]). The polaronic density obtained in the double-well scenario exhibits distinct oscillations in the  $y$  direction. The width of these oscillating peaks is much smaller than the localization length of the PBEsol[exp] in the same direction. Hence, in the case of PBEsol[exp] and PBEsol, the polaron can be considered one-dimensional and is delocalized in the  $x$  and  $z$  directions, which may correspond to the experimentally found large one-dimensional polaron of Ref. [23]. To distinguish between the two cases, flat-band or double-well potential, analysis of the characteristic dimensions and formation energies of the possible polarons is provided in the following subsection.

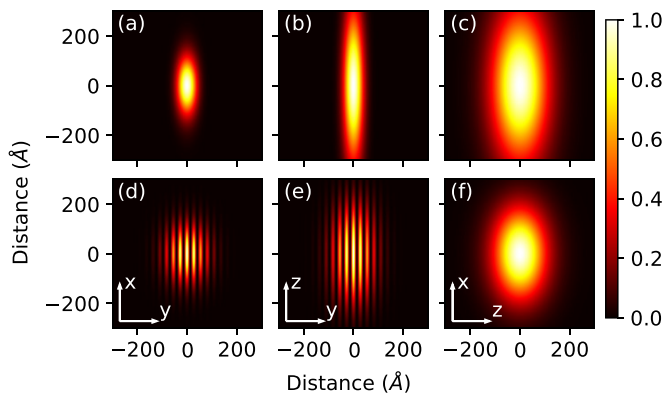


FIG. 8. Cross section of the real space polaronic density for the (a)–(c) flat-band PBEsol-exp and (d)–(f) double-well PBEsol-relaxed electronic dispersion. In all panels, the third coordinate is perpendicular to the plane and set to 0.

#### D. Analysis of the polaronic wave functions

To characterize possible polarons, along with the aforementioned variational methodology, we also utilize a trial wave-function approach. While the polaron in the flat-band scenario can be described by the ansatz of Eq. (13), the same Gaussian shape cannot be used to approximate the polaron in the double-well potential. On the contrary, one still can benefit from an *ad hoc* trial wave function: from Figs. 7(d)–7(f), we deduce that in reciprocal space it may be expressed as two Gaussians, separated by  $\Delta k$  from the origin in the  $k_y$  direction,

$$\phi(\mathbf{k}) = C \left( e^{-\frac{1}{2}(a_{p_x}^2 k_x^2 + a_{p_y}^2 (k_y - \Delta k)^2 + a_{p_z}^2 k_z^2)} + e^{-\frac{1}{2}(a_{p_x}^2 k_x^2 + a_{p_y}^2 (k_y + \Delta k)^2 + a_{p_z}^2 k_z^2)} \right), \quad (20)$$

with  $C$  being the normalization constant.

Fourier transform allows one to obtain the wave function in real space, which indeed has characteristic oscillations modulated by the cosine factor:

$$\phi(\mathbf{r}) = \left( \frac{2}{\pi^{3/2} a_p^3 (1 + e^{-\Delta k^2 a_p^2})} \right)^{1/2} e^{-\frac{1}{2} \left( \frac{x^2}{a_{p_x}^2} + \frac{y^2}{a_{p_y}^2} + \frac{z^2}{a_{p_z}^2} \right)} \cos(\Delta k \cdot y). \quad (21)$$

The electron-phonon energy to be minimized is then given as the sum of electronic and vibrational plus electron-phonon contribution, Eq. (4), with Eq. (5) [or Eq. (12) replaced by

$$E_{el}[\phi(\mathbf{k})] = \int d\mathbf{k} \varepsilon(\mathbf{k}) |\phi(\mathbf{k})|^2, \quad (22)$$

where  $\varepsilon(\mathbf{k})$  has the form of Eq. (19). It should be noted that it is possible to provide suitable polynomial expression for  $\varepsilon(\mathbf{k})$  similar to Eq. (12) and hence get an analytical result for the electronic energy term. However, since the fine features of the dispersion affect the final result, we preserve them by interpolating the bands on first-principles values in each direction. A closed-form expression for the vibrational plus electron-phonon term is not extracted, as in general the triple integral in Eq. (8) cannot be evaluated analytically, but only reduced to a double integral. Therefore, we deal with numerical integration and minimization, which can be easily performed. The aforementioned formalism is further developed in Sec. III of the Supplemental Material.

As expected, exact numerical solutions given by the variational framework result in lower values of  $E_p$ . The resulting energies obtained with variational and ansatz approaches are listed in Table XII, as well as optimized localization lengths for the latter. PBEsol[exp] and  $G_0W_0$  are approximated with the standard ansatz given by Eq. (13), while for PBEsol we use the expression given by Eq. (20). We also treat a special case (PBEsol\*) by putting a single Gaussian at one of the double-well minima and expressing the wave function with only one of the terms of Eq. (20). The listed value of  $a_{p_y}$  for PBEsol is the width of the Gaussian envelope in Eq. (21). The actual localization length  $\Delta a$  is given by the width of individual oscillations, which is determined by the  $\Delta k$  oscillatory factor in Eq. (21):

$$\Delta a_y = \frac{\pi}{2} (\Delta k)^{-1}. \quad (23)$$

Indeed, the double-well wave function has several zeros in the  $y$  direction, that in ansatz method are separated by exactly

TABLE XII. Polaron formation energy  $E_p$  in and localization lengths. Localization length are obtained with different trial wave functions: PBEsol—*ad hoc* ansatz with two Gaussians centered at each minima; PBEsol\*—single Gaussian centered at one of the minima; PBEsol[exp] and  $G_0W_0$ —standard Gaussian ansatz.

Method	$E_p$ (meV)		Localization length ( $\text{\AA}$ )		
	Variational	Ansatz	$a_{p_x}$	$a_{p_y}$	$a_{p_z}$
PBEsol	-0.65780	-0.623874	117.38	95.67	174.10
PBEsol*		-0.623177	117.60	95.87	174.27
PBEsol[exp]	-0.41774	-0.380217	132.03	42.53	366.51
$G_0W_0$ @PBEsol	-0.25635	-0.252171	181.22	128.82	451.78

$2\Delta a_y = 29.40 \text{ \AA}$ . Additionally, the PBEsol\* case gives more insight on polaron formation in the double-well scenario. Since a single Gaussian being centered at only one of the minima gives almost the same value of  $E_p$ , albeit slightly larger, we conclude that the actual polaron wave function is indeed quite similar to a superposition of two Gaussians. The polaron localization length is solely determined by the separation of the peaks, and with  $\Delta k \rightarrow \infty$  the wave function tends to its Gaussian envelope.

In Fig. 9, two polarons with the lowest localization lengths are compared: flat-band PBEsol[exp] and double-well PBEsol. Trial wave functions approximate the variational ones relatively well, with deviations arise as the distance increases. Indeed, in the exact numerical solution for PBEsol, the first peak near the origin coincides with the ansatz approach, while the width of other oscillations slowly grows with the distance. We hypothesize that experiments might detect some characteristic feature for such a polaron with approximately

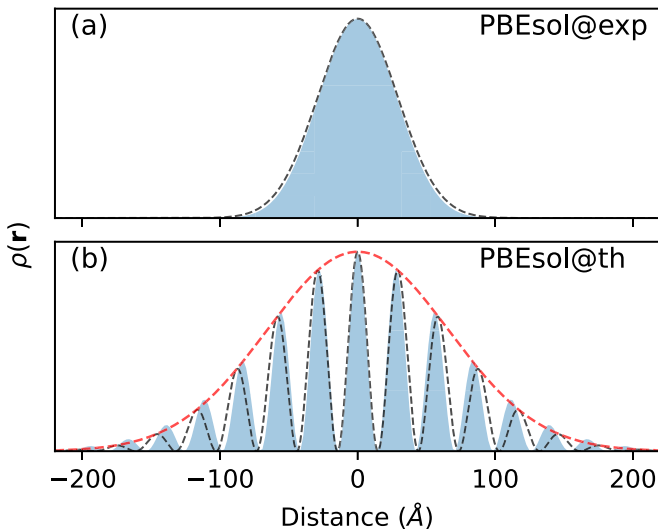


FIG. 9. Cross section of the variational (filled area) and ansatz (dashed lines) electronic density in the  $y$  direction for (a) PBEsol[exp] and (b) PBEsol. Black dashed lines denote the result from an optimized trial wave function, while the red line shows the Gaussian envelope in the double-well case. The deviation between the black dashed line and the filled area is rather small, although it increases for larger distances.

the width of the first peak or its width at half maximum,  $\Delta a_y = 14.70 \text{ \AA}$ . It is more localized than the one with the flat-band scenario. Alternatively, the separation between the zeros of the oscillating density might possibly be the characteristic length observed experimentally, with a doubled value, on the order of 3 nm. Given the uncertainty in the theoretical estimate, either one or the other may correspond to the experimentally observed one-dimensional polaron with localization length of  $18.70 \text{ \AA}$  [23]. The experimental feature hypothesized to arise from a “small” polaron with a three-dimensional character is not explained by our study: no characteristic length smaller than 1.5 nm stems from it, casting some doubts about the interpretation of experimental data.

## VII. CONCLUSIONS

In this paper, we have addressed the subtle character of the electronic structure of orthorhombic SnSe via various methodologies spanning from conventional KS-DFT mean-field approximations to state-of-the-art many-body perturbation approaches within the  $G_0W_0$  approximation for the electron-electron interaction. We have analyzed the important role played by the crystal structure in defining the topology of the electronic band structure and the effective masses. The effect is especially critical at the level of the effective masses since it plays a central role in determining large polaron properties. We have also analyzed the vibrational properties of orthorhombic SnSe to identify the phonon modes contributing to a potential polaron formation within the Fröhlich formalism.

Linking the electronic and phonon structure, we characterize the polaron energy by two different approaches: the recently developed generalized Fröhlich model and the non-adiabatic AHC formalism. We reason, based on the quantitative agreement between the two methodologies, that the polaron is of a Fröhlich type.

Based on the analyzed band extrema, we establish that the minimum of the CB at the  $\Gamma$  point could potentially hold a large polaron with a size in the range of the experimental findings. We address this aspect following two approaches: a fixed Gaussian ansatz and a variational approach both within the Fröhlich formalism. When the electronic structure presents a double-well minimum around  $\Gamma$ , we find an exotic large cylindrical one-dimensional polaron of a different type. In such a case, the oscillating electronic charge density of the polaron presents a periodicity of 3 nm and width at half maximum of 1.5 nm, which is comparable with the experimental value of 1.87 nm. Finally, we hypothesize that such type of polaron presenting an oscillatory behavior might be found in materials with extended, shallow, double-well band extrema.

Data will be made available upon request.

## ACKNOWLEDGMENTS

We thank C. Draxl and F. Caruso for discussions about the SnSe phonon nomenclature. This work has been supported by the Fonds de la Recherche Scientifique (FRS-FNRS Belgium) through the PdR Grant No. T.0103.19-ALPS. V.V. acknowledges funding by the FRS-FNRS Belgium through the

FRIA grant. Computational resources have been provided by the supercomputing facilities of the Université Catholique de Louvain (CISM/UCL), the Consortium des Equipements de Calcul Intensif en Fédération Wallonie Bruxelles (CECI) funded by the FRS-FNRS under Grant No. 2.5020.11.

B.G. performed the ground-state, MBPT, DFPT, and fixed Gaussian ansatz calculations. V.V. developed the code and

performed the variational ansatz calculation. X.G. conceptualized, supervised, coordinated, and provided funding for this work. All authors were involved in writing and reviewing the paper.

The authors declare that they have no known competing financial interests or personal relationships that could have appeared to influence the work reported in this paper.

- 
- [1] L.-D. Zhao, S.-H. Lo, Y. Zhang, H. Sun, G. Tan, C. Uher, C. Wolverton, V. P. Dravid, and M. G. Kanatzidis, *Nature (London)* **508**, 373 (2014).
- [2] R. Guo, X. Wang, Y. Kuang, and B. Huang, *Phys. Rev. B* **92**, 115202 (2015).
- [3] K. Kutorasinski, B. Wiendlocha, S. Kaprzyk, and J. Tobola, *Phys. Rev. B* **91**, 205201 (2015).
- [4] C. Chang, M. Wu, D. He, Y. Pei, C.-F. Wu, X. Wu, H. Yu, F. Zhu, K. Wang, Y. Chen, L. Huang, J.-F. Li, J. He, and L.-D. Zhao, *Science* **360**, 778 (2018).
- [5] V. Tayari, B. V. Senkovskiy, D. Rybkovskiy, N. Ehlen, A. Fedorov, C.-Y. Chen, J. Avila, M. Asensio, A. Perucchi, P. di Pietro, L. Yashina, I. Fakih, N. Hemsworth, M. Petrescu, G. Gervais, A. Grüneis, and T. Szkopek, *Phys. Rev. B* **97**, 045424 (2018).
- [6] C. Zhou, Y. K. Lee, Y. Yu, S. Byun, Z.-Z. Luo, H. Lee, B. Ge, Y.-L. Lee, X. Chen, J. Y. Lee, O. Cojocar-Mirédin, H. Chang, J. Im, S.-P. Cho, M. Wuttig, V. P. Dravid, M. G. Kanatzidis, and I. Chung, *Nat. Mater.* **20**, 1378 (2021).
- [7] R. L. González-Romero, A. Antonelli, and J. J. Meléndez, *Phys. Chem. Chem. Phys.* **19**, 12804 (2017).
- [8] H. G. von Schnering and H. Wiedemeier, *Z. Kristallogr. - Cryst. Mater.* **156**, 143 (1981).
- [9] A. Dewandre, O. Hellman, S. Bhattacharya, A. H. Romero, G. K. H. Madsen, and M. J. Verstraete, *Phys. Rev. Lett.* **117**, 276601 (2016).
- [10] D. Bansal, J. Hong, C. W. Li, A. F. May, W. Porter, M. Y. Hu, D. L. Abernathy, and O. Delaire, *Phys. Rev. B* **94**, 054307 (2016).
- [11] U. Aseginolaza, R. Bianco, L. Monacelli, L. Paulatto, M. Calandra, F. Mauri, A. Bergara, and I. Errea, *Phys. Rev. Lett.* **122**, 075901 (2019).
- [12] Y. Huang, S. Yang, S. Teitelbaum, G. De la Peña, T. Sato, M. Cholle, D. Zhu, J. L. Niedziela, D. Bansal, A. F. May, A. M. Lindenberg, O. Delaire, D. A. Reis, and M. Trigo, *Phys. Rev. X* **12**, 011029 (2022).
- [13] K. Zhang, K. Deng, J. Li, H. Zhang, W. Yao, J. Denlinger, Y. Wu, W. Duan, and S. Zhou, *Phys. Rev. Mater.* **2**, 054603 (2018).
- [14] Z. Wang, C. Fan, Z. Shen, C. Hua, Q. Hu, F. Sheng, Y. Lu, H. Fang, Z. Qiu, J. Lu, Z. Liu, W. Liu, Y. Huang, Z.-A. Xu, D. W. Shen, and Y. Zheng, *Nat. Commun.* **9**, 47 (2018).
- [15] J.-E. Lee, J. Hwang, M. Kang, H.-J. Joo, H. Ryu, K. Kim, Y. Kim, N. Kim, A. T. Duong, S. Cho, S.-K. Mo, C. Hwang, and I. H.-S. Yang, *Appl. Surf. Sci.* **520**, 146314 (2020).
- [16] T. Nishimura, H. Sakai, H. Mori, K. Akiba, H. Usui, M. Ochi, K. Kuroki, A. Miyake, M. Tokunaga, Y. Uwatoko, K. Katayama, H. Murakawa, and N. Hanasaki, *Phys. Rev. Lett.* **122**, 226601 (2019).
- [17] D. D. Cuong, S. H. Rhim, J.-H. Lee, and S. C. Hong, *AIP Adv.* **5**, 117147 (2015).
- [18] F. Caruso, M. Troppenz, S. Rigamonti, and C. Draxl, *Phys. Rev. B* **99**, 081104(R) (2019).
- [19] S. Michielon de Souza, H. Ordozgoith da Frota, D. M. Trichês, A. Ghosh, P. Chaudhuri, M. Silva dos Santos Gusmao, A. F. F. de Figueiredo Pereira, M. Couto Siqueira, K. Daum Machado, and J. Cardoso de Lima, *J. Appl. Crystallogr.* **49**, 213 (2016).
- [20] Z. Wang, J. Wang, Y. Zang, Q. Zhang, J.-A. Shi, T. Jiang, Y. Gong, C.-L. Song, S.-H. Ji, L.-L. Wang, L. Gu, K. He, W. Duan, X. Ma, X. Chen, and Q.-K. Xue, *Adv. Mater.* **27**, 4150 (2015).
- [21] Y. Sun, Z. Zhong, T. Shirakawa, C. Franchini, D. Li, Y. Li, S. Yunoki, and X.-Q. Chen, *Phys. Rev. B* **88**, 235122 (2013).
- [22] H. J. Zheng, W. J. Shi, C. W. Wang, Y. Y. Lv, W. Xia, B. H. Li, F. Wu, S. M. He, K. Huang, S. T. Cui, C. Chen, H. F. Yang, A. J. Liang, M. X. Wang, Z. Sun, S. H. Yao, Y. B. Chen, Y. F. Guo, Q. X. Mi, L. X. Yang, M. S. Bahramy, Z. K. Liu, and Y. L. Chen, *arXiv:2204.07214* [cond-mat.mtrl-sci] (2022).
- [23] L. P. R. de Cotret, M. R. Otto, J.-H. Pöhls, Z. Luo, M. G. Kanatzidis, and B. J. Siwick, *Proc. Natl. Acad. Sci.* **119**, e2113967119 (2022).
- [24] C. Franchini, M. Reticcioli, M. Setvin, and U. Diebold, *Nat. Rev. Mater.* **6**, 560 (2021).
- [25] L. D. Landau, *Phys. Z. Sowjetunion* **3**, 644 (1933).
- [26] S. I. Pekar, *Zh. Eksp. Teor. Fiz.* **16**, 341 (1946).
- [27] L. D. Landau and S. I. Pekar, *Zh. Eksp. Teor. Fiz.* **18**, 419 (1948).
- [28] T. Holstein, *Ann. Phys.* **8**, 325 (1959).
- [29] T. Holstein, *Ann. Phys.* **8**, 343 (1959).
- [30] H. Fröhlich, H. Pelzer, and S. Zienau, *London, Edinburgh Dublin Philos. Mag. J. Sci.* **41**, 221 (1950).
- [31] H. Fröhlich, *Proc. R. Soc. London A* **215**, 291 (1952).
- [32] H. Fröhlich, *Adv. Phys.* **3**, 325 (1954).
- [33] R. P. Feynman, *Phys. Rev.* **97**, 660 (1955).
- [34] A. S. Mishchenko, N. V. Prokof'ev, A. Sakamoto, and B. V. Svistunov, *Phys. Rev. B* **62**, 6317 (2000).
- [35] J. T. Devreese, *J. Phys.: Condens. Matter* **19**, 255201 (2007).
- [36] F. Giustino, *Rev. Mod. Phys.* **89**, 015003 (2017).
- [37] W. H. Sio, C. Verdi, S. Poncé, and F. Giustino, *Phys. Rev. Lett.* **122**, 246403 (2019).
- [38] W. H. Sio, C. Verdi, S. Poncé, and F. Giustino, *Phys. Rev. B* **99**, 235139 (2019).
- [39] J. Lafuente-Bartolome, C. Lian, W. H. Sio, I. G. Gurtubay, A. Eiguren, and F. Giustino, *Phys. Rev. Lett.* **129**, 076402 (2022).
- [40] J. C. de Abreu, J. P. Nery, M. Giantomassi, X. Gonze, and M. J. Verstraete, *Phys. Chem. Chem. Phys.* **24**, 12580 (2022).
- [41] P. B. Allen and V. Heine, *J. Phys. C* **9**, 2305 (1976).
- [42] P. B. Allen and M. Cardona, *Phys. Rev. B* **23**, 1495 (1981).

- [43] P.B. Allen and M. Cardona, *Phys. Rev. B* **27**, 4760 (1983).
- [44] X. Gonze, P. Boulanger, and M. Côté, *Ann. Phys.* **523**, 168 (2011).
- [45] S. Poncé, Y. Gillet, J. L. Janssen, A. Marini, M. Verstraete, and X. Gonze, *J. Chem. Phys.* **143**, 102813 (2015).
- [46] T. Nagayama, K. Terashima, T. Wakita, H. Fujiwara, T. Fukura, Y. Yano, K. Ono, H. Kumigashira, O. Ogiso, A. Yamashita, Y. Takano, H. Mori, H. Usui, M. Ochi, K. Kuroki, Y. Muraoka, and T. Yokoya, *Jpn. J. Appl. Phys.* **57**, 010301 (2018).
- [47] C. W. Wang, Y. Y. X. Xia, Z. Tian, J. Jiang, B. H. Li, S. T. Cui, H. F. Yang, A. J. Liang, X. Y. Zhan, G. H. Hong, S. Liu, C. Chen, M. X. Wang, L. X. Yang, Z. Liu, Q. X. Mi, G. Li, J. M. Xue, Z. K. Liu, and Y. L. Chen, *Phys. Rev. B* **96**, 165118 (2017).
- [48] I. Pletikosić, F. von Rohr, P. Pervan, P. K. Das, I. Vobornik, R. J. Cava, and T. Valla, *Phys. Rev. Lett.* **120**, 156403 (2018).
- [49] M. Okawa, Y. Akabane, M. Maeda, G. Tan, L.-D. Zhao, M. G. Kanatzidis, T. Suzuki, M. Watanabe, J. Xu, Q. Ren, M. Fujisawa, T. Kanai, J. Itatani, S. Shin, K. Okazaki, N. L. Saini, and T. Mizokawa, *Scripta Materialia* **223**, 115081 (2023).
- [50] G. Shi and E. Kioupakis, *J. Appl. Phys.* **117**, 065103 (2015).
- [51] B. Guster, P. Melo, B. A. A. Martin, V. Brousseau-Couture, J. C. de Abreu, A. Miglio, M. Giantomassi, M. Côté, J. M. Frost, M. J. Verstraete, and X. Gonze, *Phys. Rev. B* **104**, 235123 (2021).
- [52] B. Guster, P. Melo, B. A. A. Martin, V. Brousseau-Couture, J. C. de Abreu, A. Miglio, M. Giantomassi, M. Côté, J. M. Frost, M. J. Verstraete, and X. Gonze, *Phys. Rev. B* **105**, 119902(E) (2022).
- [53] V. Vasilchenko, A. Zhugayevych, and X. Gonze, *Phys. Rev. B* **105**, 214301 (2022).
- [54] A. Miglio, V. Brousseau-Couture, E. Godbout, G. Antonius, Y.-H. Chan, S. G. Louie, M. Côté, M. Giantomassi, and X. Gonze, *npj Comput. Mater.* **6**, 167 (2020).
- [55] X. Gonze, B. Amadon, G. Antonius, F. Arnardi, L. Baguet, J.-M. Beuken, J. Bieder, F. Bottin, J. Bouchet, E. Bousquet, N. Brouwer, F. Bruneval, G. Brunin, T. Cavignac, J.-B. Charraud, W. Chen, M. Côté, S. Cottenier, J. Denier, G. Geneste *et al.*, *Comput. Phys. Commun.* **248**, 107042 (2020).
- [56] X. Gonze, F. Jollet, F. Abreu Araujo, D. Adams, B. Amadon, T. Applencourt, C. Audouze, J.-M. Beuken, J. Bieder, A. Bokhanchuk, E. Bousquet, F. Bruneval, D. Caliste, M. Côté, F. Dahm, F. Da Pieve, M. Delaveau, M. Di Gennaro, B. Dorado, C. Espejo, *et al.*, *Comput. Phys. Commun.* **205**, 106 (2016).
- [57] X. Gonze and C. Lee, *Phys. Rev. B* **55**, 10355 (1997).
- [58] J. P. Perdew, A. Ruzsinszky, G. I. Csonka, O. A. Vydrov, G. E. Scuseria, L. A. Constantin, X. Zhou, and K. Burke, *Phys. Rev. Lett.* **100**, 136406 (2008).
- [59] M. van Setten, M. Giantomassi, E. Bousquet, M. Verstraete, D. Hamann, X. Gonze, and G.-M. Rignanese, *Comput. Phys. Commun.* **226**, 39 (2018).
- [60] D. R. Hamann, *Phys. Rev. B* **88**, 085117 (2013).
- [61] S. Grimme, *J. Comput. Chem.* **27**, 1787 (2006).
- [62] S. Grimme, J. Antony, S. Ehrlich, and H. Krieg, *J. Chem. Phys.* **132**, 154104 (2010).
- [63] A. D. Becke and E. R. Johnson, *J. Chem. Phys.* **124**, 221101 (2006).
- [64] J. Heyd, G. E. Scuseria, and M. Ernzerhof, *J. Chem. Phys.* **118**, 8207 (2003).
- [65] I. Souza, N. Marzari, and D. Vanderbilt, *Phys. Rev. B* **65**, 035109 (2001).
- [66] X. Gonze, G. M. Rignanese, and R. Caracas, *Z. Kristallogr.* **220**, 458 (2005).
- [67] J. Laflamme Janssen, Y. Gillet, S. Poncé, A. Martin, M. Torrent, and X. Gonze, *Phys. Rev. B* **93**, 205147 (2016).
- [68] P. Ghosez, J. P. Michenaud, and X. Gonze, *Phys. Rev. B* **58**, 6224 (1998).
- [69] F. Bruneval and X. Gonze, *Phys. Rev. B* **78**, 085125 (2008).
- [70] W. E. Pickett, H. Krakauer, and P. B. Allen, *Phys. Rev. B* **38**, 2721 (1988).
- [71] S. Grimme, S. Ehrlich, and L. Goerigk, *J. Comput. Chem.* **32**, 1456 (2011).
- [72] K. Adouby, C. Pérez-Vicente, J. C. Jumas, R. Fourcade, and A. A. Touré, *Z. Kristallogr. - Cryst. Mater.* **213**, 343 (1998).
- [73] H. R. Chandrasekhar, R. G. Humphreys, U. Zwick, and M. Cardona, *Phys. Rev. B* **15**, 2177 (1977).
- [74] T. Chattopadhyay, J. Pannetier, and H. Von Schnering, *J. Phys. Chem. Solids* **47**, 879 (1986).
- [75] Q. Lu, M. Wu, D. Wu, C. Chang, Y.-P. Guo, C.-S. Zhou, W. Li, X.-M. Ma, G. Wang, L.-D. Zhao, L. Huang, C. Liu, and J. He, *Phys. Rev. Lett.* **119**, 116401 (2017).
- [76] See Supplemental Material at <https://link.aps.org/supplemental/10.1103/PhysRevMaterials.7.064604> for the electronic dispersion figures comparing different structures and different XC functionals, as well as the formalism for the double-well approach.
- [77] H. Mori, H. Usui, M. Ochi, and K. Kuroki, *Phys. Rev. B* **96**, 085113 (2017).
- [78] F. Liu, P. Parajuli, R. Rao, P. C. Wei, A. Karunaratne, S. Bhattacharya, R. Podila, J. He, B. Maruyama, G. Priyadarshan, J. R. Gladden, Y. Y. Chen, and A. M. Rao, *Phys. Rev. B* **98**, 224309 (2018).
- [79] C. W. Li, J. Hong, A. F. May, D. Bansal, S. Chi, T. Hong, G. Ehlers, and O. Delaire, *Nat. Phys.* **11**, 1063 (2015).
- [80] G. D. Mahan, *Many-Particle Physics*, 3rd ed. (Kluwer, New York, 2000).